Theoret. Comput. Fluid Dynamics (1998) 11: 281–303

Theoretical and Computational Fluid Dynamics

Turbulent Dynamics of a Critically Reflecting Internal Gravity Wave[1]

Donald N. Slinn[2] and J.J. Riley

Department of Mechanical Engineering,
University of Washington,
Seattle, WA 98195, U.S.A.

Communicated by J.R. Herring

Received 21 May 1997 and accepted 14 October 1997

Abstract. Results from computational fluid dynamics experiments of internal wave reflection from sloping boundaries are presented. In these experiments the incident wave lies in a plane normal to the slope. When the angle of wave energy propagation is close to the bottom slope the reflection causes wave breakdown into a quasi-periodic, turbulent boundary layer. Boundary layer energetics and vorticity dynamics are examined and indicate the importance of the three-dimensional turbulence. The boundary layer exhibits intermittent turbulence: approximately every 1.2 wave periods the boundary layer mixes energetically for a duration of about one-third of a wave period, and then it restratifies until the next mixing event. Throughout the wave cycle a strong thermal front is observed to move upslope at the phase speed of the incident waves. Simulations demonstrate that the net effects of turbulent mixing are not confined to the boundary layer, but are communicated to the interior stratified fluid by motions induced by buoyancy effects and by the wave field, resulting in progressive weakening of the background density gradient. Transition to turbulence is determined to occur at Reynolds numbers of approximately 1500, based upon the wavelength and maximum current velocity of the oncoming wave train. The boundary layer thickness depends on the Reynolds number for low Richardson numbers, with a characteristic depth of approximately one-half of the vertical wavelength of the oncoming wave.

1. Introduction

Recent field experiments (Eriksen, 1985, 1998) have suggested that the oceanic internal wave field can provide sufficient energy to activate strong mixing near sloping boundaries, which can in turn account for a significant portion of the overall oceanic vertical mixing. One mechanism by which this may occur is the breaking of internal gravity waves as they reflect off the continental shelf, or off other sloping boundaries near islands or seamounts. Many dynamical properties of internal gravity waves are well understood and accurately described by linear theory, and this theory has been applied to internal wave reflection, e.g., Phillips (1977), Gordon (1980), and Eriksen (1985). More extensive theoretical models that include interactions between

[1] This work was supported primarily under U.S. Navy Office of Naval Research (ONR) Contract N00014-90-J-1112. Support was also provided for D.N.S. as a Post-Doctoral researcher by ONR Contract N00014-95-1-0047 through a grant to J.S. Allen and R.A. Holman at Oregon State University. Supercomputer support was obtained from the National Center for Supercomputer Applications at the University of Illinois, Urbana-Champagne and by the College of Oceanic and Atmospheric Sciences, OSU through a grant to M.R. Abbott from the NASA-EOS program.

[2] Present affiliation: College of Oceanic and Atmospheric Sciences, Oregon State University, Oceanography Administration Building 104, Corvallis, OR 97331-5503, U.S.A.

oncoming and reflected waves have been developed to explain resonant forcing, the development of nonlinearities, and topographic influences, e.g., Thorpe and Haines (1987), Gilbert and Garrett (1989), and Thorpe (1989, 1997). The situation probably most effective for boundary mixing arises when an oncoming wave reflects from a bottom slope α that nearly matches the angle of wave propagation θ. In this case linear theory suggests that a small amplitude oncoming wave may be reflected with large amplitude, thus exhibiting nonlinear behavior and possibly wave breaking and turbulence. The flux of reflected energy from the slope is adjusted in two ways during reflection. The wave energy is transferred to shorter wavelength (higher wave-number), and the group velocity decreases. At the critical condition, $\theta = \alpha$, linear wave theory predicts a reflected wave of infinite amplitude, infinitesimal wavelength, and zero group velocity, leading to the trapping of oncoming wave energy in the boundary region. In such a case, nonlinearities and turbulence must come into play.

Observations of the oceanic internal wave field near sloping bottom topography by Eriksen (1982) have drawn attention to the probable role of wave-induced mixing in boundary layers with thicknesses of approximately 100 m. Observations of spectral enhancement of the internal wave energy are centered about the critical frequency associated with the bottom slope, and occur over the breadth of frequency range expected from linear theory. Amplitudes of the reflected waves, however, are much smaller than linear theory predicts. The differences have been attributed to frictional dissipation near the boundary and to highly nonlinear interactions. Evidence of wave breaking in the boundary layer (Eriksen, 1998) has also been found, but the instability mechanism, whether shear-induced (e.g., Kelvin-Helmholtz) or convective (buoyancy-induced) instability, has not been determined. In other field observations strong density gradients have been measured (Thorpe, 1992), and frequent overturns of stratified fluid were observed (Eriksen, 1998), suggesting large diffusivities associated with the boundary layers. In addition, wave amplification has been suggested as the source of strong boundary shear stresses that cause persistent sediment suspension on the continental shelf (Cacchione and Drake, 1986).

Laboratory experiments of internal wave reflection (Cacchione and Wunsch, 1974; Cacchione and Southard, 1974) demonstrate that wave amplification is in good agreement with linear theory, for cases sufficiently far from the critical angle. Near the critical angle the reflected wave amplitudes are much less than those predicted by linear theory, and the boundary layer is characterized by a turbulent bore surging upslope, reminiscent of a breaking surface wave on a beach. Ivey and Nokes (1989) and Taylor (1993) observe that, for critical reflection, the boundary layer may exhibit steady or unsteady turbulence depending on the bottom slope. They find the boundary layer thickness and the mixing efficiency (the portion of wave energy converted to potential energy through turbulent mixing) are linearly related to the incident wave amplitude A_{w} up to an upper bound at which A_{w} exceeds about one-tenth of the amplitude of an overturning wave.

Several questions remain concerning the behavior of internal wave reflection from sloping boundaries. How do nonlinearity and diffusion influence wave reflection near critical conditions? What types of instabilities are present in the flow and how do the waves transition to turbulence? What physical mechanisms are responsible for the distribution of vorticity in the boundary layer? Into what form of energy is the wave energy converted when the wave has broken down? Are mean currents or steady circulations induced near the slope? How is the background density profile affected away from the boundary? Is mixed fluid in the boundary layer communicated to the interior stratified regions? In this paper we attempt to address these questions by reporting on some numerical experiments.

We utilize numerical simulations of the Navier–Stokes equations to complement previous methods of investigation. The advantage of this methodology over previous use of linear inviscid theory is the ability to include nonlinear and diffusive effects in the model; the advantage over laboratory experiments is the ability to make available detailed information on the flow field, allowing one to address the energetics and turbulence dynamics in detail, and to facilitate flow measurement and visualizations. The paper is organized into four sections. The model and problem formulation are described briefly in Section 2, results from the numerical experiments are presented in Section 3, and Section 4 contains the summary and conclusions.

2. Model Description

When an internal wave of frequency ω propagating in a uniformly stratified environment reflects from a larger-scale, sloping boundary, its angle of propagation with respect to the horizontal, θ, is preserved

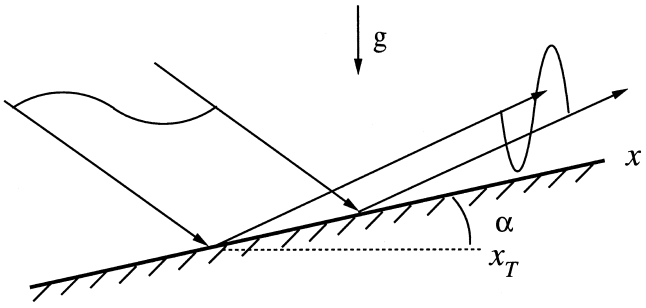

Figure 1. Ray tube reflection diagram for internal gravity waves reflecting from a sloping boundary.

(Phillips, 1977). The angle between the group velocity vector and the horizontal depends upon the wave frequency, ω, and the background density stratification according to the dispersion relation $\omega = N \sin\theta$, where N is the buoyancy frequency defined by $N^2 = (-g/\rho_0)(\partial\overline{\rho}/\partial z_T)$, where z_T is in the direction opposite the gravity vector. Figure 1 shows the wave reflection process using a ray-tube diagram based upon linear theory, and illustrates the basic problem geometry. Here α is the angle that the sloping boundary makes with the horizontal, g is the direction of gravity, the x-direction is alongslope, the x_T-direction is horizontal, and the z-direction is perpendicular to the sloping boundary. This reflection from a sloping boundary can lead to an increase in the energy density of the wave, as the energy in the oncoming wave is concentrated into a more narrow ray tube upon reflection.

The numerical model is described in detail in a separate paper (Slinn and Riley, 1998a) and preliminary results have been reported (Slinn and Riley, 1996). The model simulates forced, dissipative, incompressible flow within the Boussinesq approximation (Phillips, 1977), in which the governing equations are written in terms of pressure and density fluctuations with the hydrostatic balance removed. The model is periodic in the x- and y-directions and bounded by a plane wall at the bottom boundary (see Figure 2). For a sloping ocean floor, the coordinate system used in the numerical simulation is rotated as shown. Note that the background density and pressure fields are not periodic at the lateral boundaries in x. Since the background fields have been subtracted from the governing equations, however, if the remaining perturbation density and pressure fields are initially periodic in the x-direction, they will remain so.

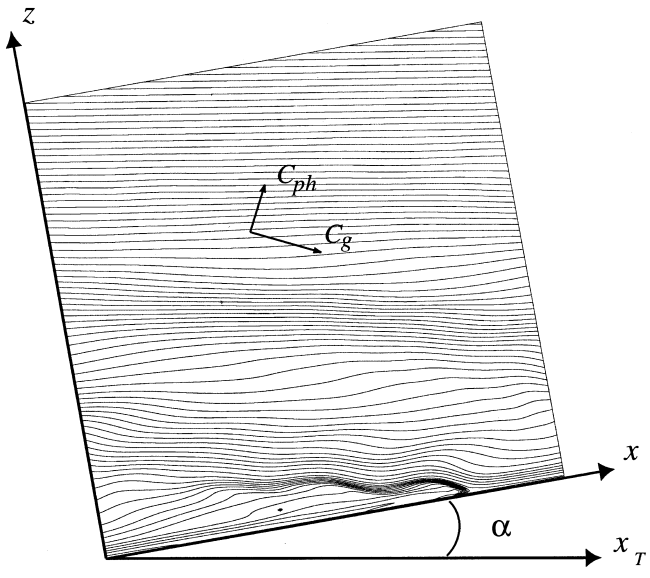

Figure 2. Density contours for an oncoming wave train (generated in a forcing region above the bottom boundary) propagate downward with phase and group velocities as indicated for Experiment 1 at t = 73.

The nondimensionalized governing equations in a coordinate system rotated through angle α with respect to the vertical are

$$\nabla \cdot \mathbf{u} = 0 \,, \tag{2.1}$$

$$\frac{\partial u}{\partial t} + \mathbf{u} \cdot \nabla u + Ri\rho \sin\alpha = -\frac{\partial p}{\partial x} + \frac{1}{Re}\nabla^2 u + F_u \,, \tag{2.2}$$

$$\frac{\partial v}{\partial t} + \mathbf{u} \cdot \nabla v = -\frac{\partial p}{\partial y} + \frac{1}{Re}\nabla^2, \tag{2.3}$$

$$\frac{\partial w}{\partial t} + \mathbf{u} \cdot \nabla w + Ri\rho \cos\alpha = -\frac{\partial p}{\partial z} + \frac{1}{Re}\nabla^2 w + F_{\mathrm{w}}, \tag{2.4}$$

$$\frac{\partial \rho}{\partial t} + \mathbf{u} \cdot \nabla \rho - w\cos\alpha - u\sin\alpha = \frac{1}{PrRe}\nabla^2 \rho + F_\rho. \tag{2.5}$$

The nondimensional parameters, the Richardson, Reynolds, and Prandtl numbers, are

$$Ri = \left(\frac{NL}{U}\right)^2, \qquad Re = \frac{UL}{\nu}, \qquad Pr = \frac{\nu}{\kappa}, \tag{2.6a–c}$$

where L and U are characteristic length and velocity scales, respectively, and ν and κ are the diffusivities of momentum and density, and ρ is nondimensionalized by $L\partial\overline{\rho}/\partial z$.

During simulations, incoming waves are forced continuously from inside the computational domain, utilizing the forcing terms on the right-hand sides of the governing equations. Both the velocity and density fields are locally forced in a manner that generates a monochromatic wave train with specified frequency and wavenumber vector incident upon the sloping terrain. The forcing functions in the rotated coordinate system are specified using the relations

$$F_u = -\frac{Am}{k}F(z)\cos(kx + mz - \omega t) - \frac{A}{k}F'(z)\sin(kx + mz - \omega t), \tag{2.7}$$

$$F_{\mathrm{w}} = AF(z)\cos(kx + mz - \omega t), \tag{2.8}$$

$$\begin{aligned} F_\rho = {} & \frac{-A\cos\alpha F(z)}{\omega}\sin(kx + mz - \omega t) + \frac{Am\sin\alpha F(z)}{\omega k}\sin(kx + mz - \omega t) \\ & - \frac{A\sin\alpha F'(z)}{\omega k}\cos(kx + mz - \omega t). \end{aligned} \tag{2.9}$$

Following Winters (1989), the localization function $F(z)$ is

$$F(z) = \exp[-b(z - z_0)^2], \qquad 0 \le z \le L_z, \tag{2.10}$$

where L_z is the height of the computational domain in z, and the forcing is centered at $z_0 = 2L_z/3$. Note that the forcing implies that the oncoming wave is in the vertical plane defined by the normal to the boundary.

We show elsewhere (Slinn and Riley, 1998a) that a monochromatic wave train of constant amplitude, A_{c}, is emitted from the wave forcing region described by the relations

$$u = -\left(\frac{A_{\mathrm{c}}m}{k}\right)\cos(kx + mz - \omega t), \tag{2.11a}$$

$$w = A_{\mathrm{c}}\cos(kx + mz - \omega t), \tag{2.11b}$$

$$\rho = \left(\frac{-A_{\mathrm{c}}\cos\alpha}{\omega} + \frac{A_{\mathrm{c}}m\sin\alpha}{k\omega}\right)\sin(kx + mz - \omega t) \tag{2.11c}$$

where $\omega^2 = Ri(k\cos\alpha - m\sin\alpha)^2/(k^2 + m^2)$. The velocity scale U for nondimensionalizing the problem is the maximum current speed in the oncoming wave $(u^2 + w^2)^{1/2}$, and the length scale L is the wavelength in the direction of the wave-number vector $k\hat{i} + m\hat{k}$. For convenience we define the wave amplitude A_{c} in relation to the wave amplitude of an overturning wave, A_{o}, at which there is a vanishing density gradient in the direction opposite the gravity vector at the steepest point of the wave, e.g., $\partial\rho_{\mathrm{t}}/\partial z_T = 0$, where ρ_{t} is

defined immediately below. This leads to the condition that $A_c = A_o = \omega/(m\cos\alpha + k\sin\alpha)$ at the point of incipient wave overturning.

No-slip boundary conditions on velocity are employed at the bottom boundary, while a zero flux boundary condition is used for the density field,

$$\frac{\partial \rho}{\partial z} = -\cos\alpha \qquad \text{at} \quad z = 0, \tag{2.12}$$

where the total density field in the rotated coordinate system is $\rho_t = \rho_0 - \cos\alpha z - \sin\alpha x + \rho$. Above the wave forcing region is a numerical open boundary condition utilizing a Rayleigh damping sponge layer (Durran *et al*., 1993) that absorbs outgoing wave energy with minimal reflection.

For the higher Reynolds number experiments, e.g., for $Re > 2000$ (presented in the next section), the model incorporates additional artificial numerical dissipation at the smallest resolved length scales. This is accomplished by adding hyperviscosity terms, e.g., $\mu\nabla^6\mathbf{u}$, $\mu\nabla^6\rho$ with $\mu \ll 1$, to the momentum and density equations to filter energy at poorly resolved scales of motion. The method incorporates the compact filtering techniques of Lele (1992) and is presented in detail in Slinn and Riley (1998a). Since internal wave reflection is not microscale driven, modeling of small-scale dissipation with a hyperviscosity does not dominate or invalidate the useful information derived from the results.

For analysis of the experiments we use the volume-averaged kinetic, potential, and total energy equations. The kinetic energy is defined by $(u^2 + v^2 + w^2)/2$, the potential energy by $Ri\rho^2/2$ (Winters *et al.*, 1995), and the total energy is their sum. Consider the equation for the volume-averaged kinetic energy, defined for a control volume extending from the sloping boundary to the base of the sponge layer:

$$\frac{\partial KE}{\partial t} = \frac{1}{V}\int_V [B_f + \epsilon + F_{KE} + W_{KE}]\,dV + \frac{1}{L_x L_y}\int_0^{L_x}\int_0^{L_y} [(w\cdot KE)|_{z=top} + (w\cdot p)|_{z=top}]\,dx\,dy. \tag{2.13}$$

Here F_{KE} is the dissipation of kinetic energy by the hyperviscosity filter, ε is the kinetic energy dissipation rate (Batchelor, 1967), the buoyancy flux is $B_f = Ri\rho(w\cos\alpha + u\sin\alpha)$, and the work input by the wave forcing mechanism is $W_{KE} = uF_u + wF_w$. The last two terms represent the advective and radiative fluxes, respectively, of kinetic energy through the upper boundary of the control volume.

The volume averaged potential energy equation is

$$\frac{\partial PE}{\partial t} = \frac{1}{V}\int_V [-B_f + \chi + F_{PE} + W_{PE}]\,dV + \frac{1}{L_x L_y}\int_0^{L_x}\int_0^{L_y} [(w\cdot PE)|_{z=top}]\,dx dy. \tag{2.14}$$

Here F_{PE} is the dissipation of potential energy by the filter, χ is the potential energy dissipation rate (Winters *et al.*, 1995), and $W_{PE} = Ri\rho F_\rho$ is the work input from the wave forcing mechanism. The last term represents the advective flux of potential energy through the upper boundary of the control volume.

Low-level white noise is included as part of the initial conditions, and the internal wave forcing is started from rest at $t = 0$. After a short startup period a quasi-steady flow develops in which a beam of sinusoidal internal waves propagate toward, and interacts with, the bottom boundary. Figure 2 shows isopycnals of finite amplitude waves emerging from the region of wave forcing, approaching, and interacting with the sloping bottom boundary. The figure is a two-dimensional (x, z) cross section from a three-dimensional simulation.

3. Results

Concepts about wave reflection and boundary layer development are examined by presenting results from an experiment in detail. Experiments with different bottom slopes are reported in Slinn and Riley (1998a,b). The present experiment is a critical angle simulation with a bottom slope of 9.2°, a Reynolds number of $Re = 3600$, based upon the wavelength λ and the maximum current speed U of the oncoming wave, and Richardson number $Ri = (N\lambda/U)^2 = 46$. The three-dimensional computation uses $129 \times 65 \times 130$ grid points in the x-, y-, and z-directions. Figure 3 shows a time sequence of constant density surfaces depicting the flow during a period of wave breakdown. Each panel of Figure 3 focuses on the near-wall

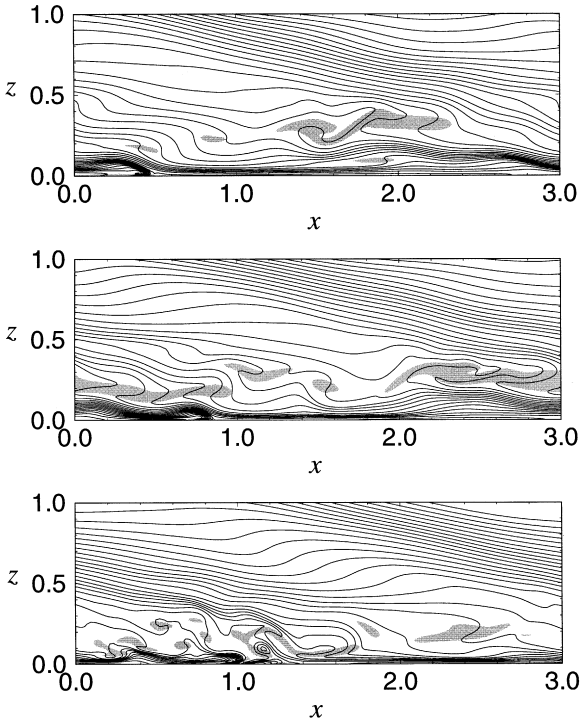

Figure 3. Density fields with statically unstable overturned regions at t = 88.5 (top), 93.7 (middle), and 102.2 (bottom) shown shaded. The dimensions of the panels are one vertical wavelength, λ_z, in the z-direction by one horizontal wavelength, λ_x, in x-direction. The panels should be rotated counterclockwise 9.2° to orient the gravity vector vertically. Contours are shown at intervals of 0.05, where the background density gradient $\partial\overline{\rho}/\partial z = -\cos\alpha$.

region corresponding to the bottom portion of Figure 2. For the oncoming internal wave $\lambda_x = 3\lambda_z$, where λ_x and λ_z refer to the wavelengths in the x- and z-directions. The dimension of the figures are λ_x in x and λ_z in z. The wavelength in the direction of the wave-number vector is $\lambda = 0.95\lambda_z$, according to the relation $1/\lambda^2 = 1/\lambda_x^2 + 1/\lambda_z^2$. Time is nondimensionalized by the buoyancy frequency, N, the wave period is 39.2, and the buoyancy period is 2π.

In the lower left corner of the panels a strong gradient in density is observed. This feature, called a thermal front by Thorpe (1992), moves upslope at the x component of the phase speed of the oncoming wave. As time progresses, wave overturning develops in the lee of the thermal front, and at time t = 88.5 (top panel), statically unstable fluid (shaded area) is apparent near the center of the domain. This behavior is similar to observations of Thorpe and Haines (1987) and Taylor (1993) who observed Kelvin–Helholtz billows developing in the region of strong shear in the lee of the thermal front. In our numerical experiments the lee waves do not appear to develop all the way to Kelvin–Helholtz billows before wave overturing on a larger horizontal length scale dominates the region. We attribute the damping of the lee waves to the higher viscosity in the numerical experiments and the subsequent larger-scale density inversions to the lower Richardson numbers of our experiments. As time continues, the overturned regions break down into small-scale turbulence and dissipate the wave energy in a three-dimensional fashion; at later times, the boundary layer relaminarizes and restratifies. By t = 140 (not pictured) the flow once again becomes overturned throughout much of the boundary layer similar to the behavior at t = 93.7. The zero density flux boundary condition at the lower boundary drives a Phillips (1970) type boundary layer in a thin region very near the bottom slope too thin to be visible in Figure 3. The energy density of the Phillips flow is much lower than the energy density of the reflected wave and becomes obscured by the signal of the breakdown process. In addition, the steady-state Phillips flow takes approximately three to five buoyancy periods to establish itself in a quiescent fluid (Slinn and Riley, 1998a) and does not have time to re-establish itself fully between wave breakdown cycles.

The flow development in the boundary region is also illustrated in Figure 4. Here two-dimensional velocity vectors (from the u and w components) are shown in the same x–z plane as in Figure 3. The velocity vectors are presented on a sparse grid, scaled to enhance visibility. A reference vector with magnitude $|\mathbf{u}| = 0.35$ is include below each panel. The shear of the oncoming wave and regions of flow recirculation are evident in Figure 4. The dynamics of the wave breakdown appear to be associated with local upslope/downslope

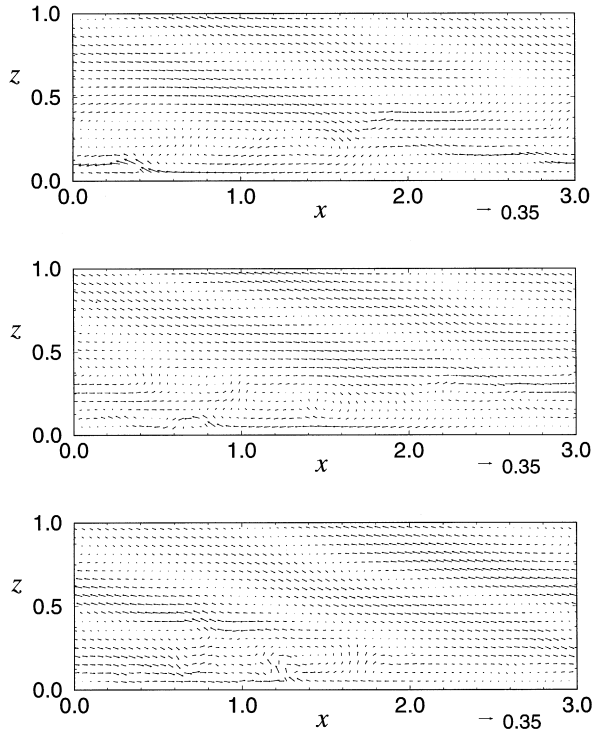

Figure 4. Velocity vectors in the boundary region for the same time sequence of flow development as Figure 3, at t = 88.5 (top), 93.7 (middle), and 102.2 (bottom).

flow induced by the oncoming wave. As the wave energy is amplified in the boundary layer strong currents result, with local velocities approximately two times larger than velocities in the wave as it approaches the boundary. It appears that the upslope flow (e.g., at t = 88.5, $z = 0.4\lambda_z$), generated by a phase of the oncoming wave interacting with the boundary, is responsible for setting up wave overturning in the boundary layer that leads to subsequent wave breakdown into turbulence.

Near the boundary, and especially above the location of the thermal front, upwelling fluid is clearly apparent. As time progresses, regions of vertically recirculating fluid appear throughout the boundary region. Additional analysis indicates that the eddies are three-dimensional in character and correlated with the location of overturned isopycnals. The eddies actively participate in strong local vertical mixing. An important feature of the flow, which shows up for many of the critically sloping cases, is apparent in the middle frame of Figure (t = 93.7): a region of downslope flow occurs very near the wall across most of the breadth of the domain. The flow is similar to the backwash produced on a beach after a wave has broken on shore, and is a type of restratification driven by buoyancy forces. The backwash behaves similar to a viscous gravity current (Turner, 1973). The leading edge of the downslope flow propagates approximately one-third of a horizontal wavelength in 0.15 wave periods before becoming obscured by the next oncoming phase of the upslope thermal wave front. For critical frequency waves, whether a backwash is present or not, nearly all the wave energy is dissipated, but when this layer exists, mixing is enhanced. MacCready and Rhines (1991) discuss similar "slippery boundary layers" and their importance to changing the bottom friction experienced by larger-scale flows.

3.1. Three-Dimensionality

The previous figures have indicated the structure of the flow in only one vertical plane. Here we examine the three-dimensional nature of the flow during wave breakdown into turbulence. Some features important to the description of turbulence include irregularity and randomness. Also, turbulent flows possess a wide range of scales of motion, and are unstable and strongly nonlinear. They are characterized by large amounts of vorticity, are highly dissipative, and have high rates of transport of mass, momentum, and scalar properties such as heat or salt. Finally, an essential component of a turbulent flow is that it is three-dimensional. This

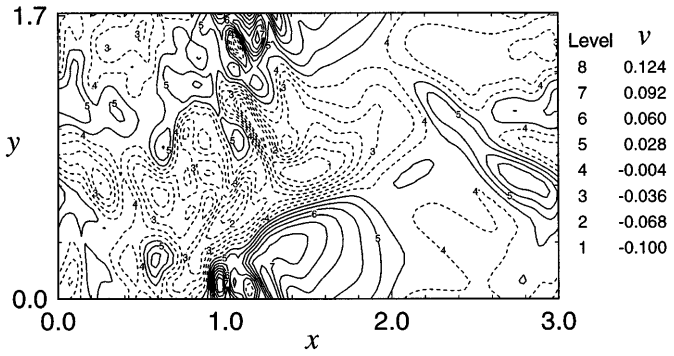

Figure 5. v-velocity contours in a plane parallel to the bottom plane at $z = 0.07\lambda_z$, within the turbulent boundary layer, at $t = 102.2$.

section presents evidence that the wave breakdown process is three-dimensional, supporting the conclusion that the two-dimensional oncoming waves transition to turbulence.

Figure 5 indicates an aspect of the three-dimensionality of the flow. Here, velocity contours of the v component of velocity are shown in the x–y plane at $z = 0.07\lambda_z$ for $t = 102.2$. There is no v component of the velocity in the oncoming wave. The strongest production of the v component is observed to occur at (and move upslope with) the location of the thermal front, leaving decaying turbulence in its wake.

Indications of the time variation of the three-dimensional aspects of the flow are given in Figure 6, which shows volume integrals of the three components of kinetic energy ($u^2/2$, $v^2/2$, and $w^2/2$). The volume integrals are summed over the entire computational domain, including the wave forcing region, and hence include energy from the oncoming wave in the u^2 and w^2 components. The magnitudes of energy in u^2 and w^2 are therefore considerably larger than v^2, and their variation during wave breakdown is less pronounced. Since the oncoming wave does not contain any v^2 component of kinetic energy, this component is a good measure of the increase of three-dimensionality in the boundary region.

During the early period, $t < 60$, as the wave train approaches the wall, the magnitude of v^2 decreases, indicating viscous decay of the initial white noise. When wave reflection begins in earnest around $t = 70$, the three-dimensionality of the flow grows rapidly. During the period of strong mixing, from about $t = 90$ to $t = 110$, kinetic energy in v^2 is strongly enhanced, increasing by a factor of approximately five. After the mixing cycle is completed, the three-dimensionality of the flow decreases rapidly and, within about two buoyancy periods ($2T_b = 12.6$), has dropped significantly. During this period of relaminarization, the flow is also being restratified (i.e., the mixed fluid settles back to a statically stable profile through a combination of diffusion and buoyancy forces). The next mixing cycle occurs near $t = 150$ and is of approximately the same strength as the previous event. Again the three-dimensionality of the flow increases significantly. The mixing cycle has a periodicity of approximately $T_m = 45$. The nonlinearities of turbulence, and other flow dynamics discussed below, may account for a departure of this time scale from the wave period of 39.2. Additional flow statistics, such as the strength of various shear components (e.g., Figure 20 below), and flow visualizations, support the finding that the duration of the mixing cycle differs from the wave period.

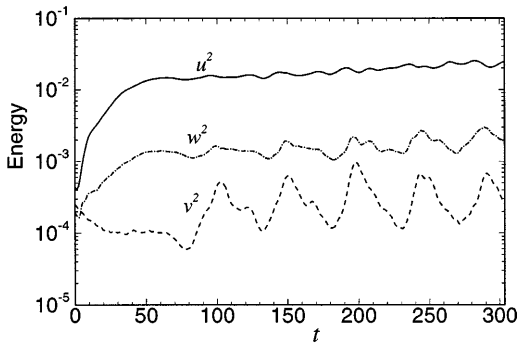

Figure 6. Volume integrals of the individual components of the kinetic energy, u^2, v^2, and w^2.

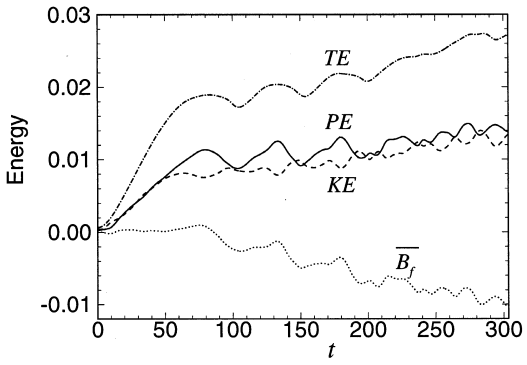

Figure 7. Volume integrals of kinetic, potential, and total energy and the time integrated buoyancy flux, $\overline{B_f}$.

Figures 5 and 6 indicate that wave breakdown becomes three-dimensional. In the sections to follow, other important aspects of the turbulence will be presented, including instabilities, intermittency, vorticity dynamics, and dissipation rates.

3.2. Energetics

While the flow exhibits characteristics of temporal periodicity, other aspects appear to achieve quasi-steady behavior. Figure 7 shows that the volume integrals of kinetic, potential, and total energies begin to approximately level off after the oncoming wave begins interacting with the boundary. Approximate equipartition of energy is observed (i.e., equal kinetic and potential energy) since the volume-integrated energy is dominated by the oncoming wave. Also shown in Figure 7 is the time-integrated buoyancy flux, $\overline{B_f}$; its negative value indicates a net transfer of potential to kinetic energy. After about $t = 60$ the energy input from the wave forcing mechanism nearly equals the dissipation of energy when averaged over a wave period.

Two types of situations have been observed in different simulations. In the first, the total energy in the system levels off after a few wave cycles, and the system reaches quasi-equilibrium as the energy oscillates about a mean value. A second observed situation is that wave breakdown establishes a mean flow and/or alters the background density profile in the boundary layer. The alteration of the background density profile appears in the energy integral as an accumulation of potential energy, because any deviation from a linear profile is considered potential energy by definition (even if it is unavailable to do work). An adjustment to the mean flow in the boundary layer will appear as an accumulation of kinetic energy. Either of these flow modifications can lead to a steady increase in the total energy in the system.

Figure 7 shows for the present case that the flow has greater potential energy than kinetic energy during each mixing phase. This is consistent with Figure 10, which shows a higher dissipation rate of kinetic energy ε than of potential energy χ. A significant cause of this difference is the different boundary conditions on each field at the bottom slope. The no-slip boundary condition creates a strong sink of kinetic energy, which is not duplicated by the no-flux boundary condition on the density field. As the wave is annihilated by turbulence and wall interaction, buoyancy effects transfer excess potential to kinetic energy. Here, the energy accumulates both as a mean flow and an adjustment to the background density profile (e.g., Figures 22 and 23 below).

Figure 8 shows the volume integrals of the various terms of the kinetic energy equation (2.13) as a function of time. The overall balance of kinetic energy has been determined to be very good: typically, errors are less than 1% of the work input. The buoyancy flux in the kinetic energy equation is plotted so that it represents a gain in kinetic energy when it is positive. Figure 8 shows that the rate of change of kinetic energy follows the buoyancy flux more closely than any other term. Over each mixing period the net input of work is roughly equal to the total dissipation. The oscillation of the work input, beginning at $t \approx 100$, is attributable to reflected waves that propagate upward from the turbulence in the boundary layer and enter into the wave generation region, modulating the local velocity field and hence the work input.

In Figure 8 the dissipation of kinetic energy by the filter has been separated from the numerically resolved dissipation. Comparison of these magnitudes shows that most of the dissipation has been resolved. The maximum energy removal by filtering occurs just after the peak in ε (e.g., $t \approx 100$, 150) when the

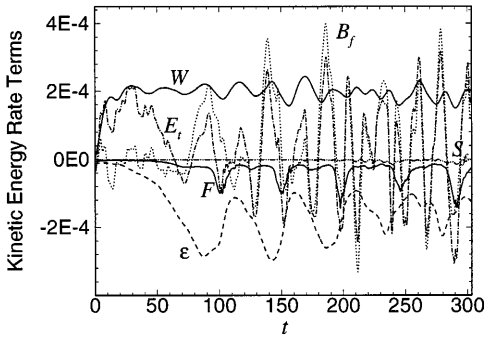

Figure 8. Volume integrals of terms in the kinetic energy equation (2.13): work input W, change in energy in time $E_{\rm t}$, dissipation rates ε, filter dissipation rate F, buoyancy flux $B_{\rm f}$, flux of energy into sponge layer $S_{\rm f}$.

turbulence has cascaded down to smaller, poorly resolved scales. Time integration of the losses of energy shows that, overall, 86% of the total kinetic energy dissipation has been achieved through ε and that 14% has been accomplished by the filter. The potential and total energy balances show similar trends. Here the resolved dissipation accounts respectively for 77% of the potential and 83% of the total energy. Thus, in this experiment a significant percentage of the total energy dissipation occurs due to the hyperviscosity filter. Terms of the potential energy equation (not shown) are similar in character to terms in the kinetic energy equation.

Figure 9 shows the terms of the total energy equation. Here, much of the complication of the preceding figure is eliminated because the buoyancy flux drops out of the total energy equation, and the balance between work input and dissipation is more readily apparent. The rate of change of total energy oscillates between positive and negative values between periods of strong mixing and dissipation, and periods of restratification and relaminarization.

Figure 10 shows the correlation that exists between the buoyancy flux and the mixing cycles. Four curves are plotted in Figure 10: the buoyancy flux $B_{\rm f}$ (positive values indicate a transfer to kinetic energy), the total potential energy dissipation rate (χ + $F_{\rm PE}$), the total kinetic energy dissipation rate (ε + $F_{\rm KE}$), and the total energy dissipation rate. Note that the dissipation rate of potential energy is only approximately one-half the dissipation rate of kinetic energy. Through the first two mixing cycles there is a strong transfer of potential to kinetic energy at the same time that the dissipation is strongest. It should be recalled that the oncoming gravity waves contain equal amounts of kinetic and potential energy. Therefore, when the waves break down in the turbulent boundary layer, and kinetic energy is dissipated more strongly than potential energy, the resulting flow adjusts by transferring potential to kinetic energy. The rapid drop in the buoyancy flux, to negative values, occurs at the same time as the mixing and dissipation decrease, near times 105 and 150. During the later mixing cycles, near times 190 and 235, the picture becomes more complex, with oscillations in the buoyancy flux occurring approximately twice per wave period. By these later times significant additional

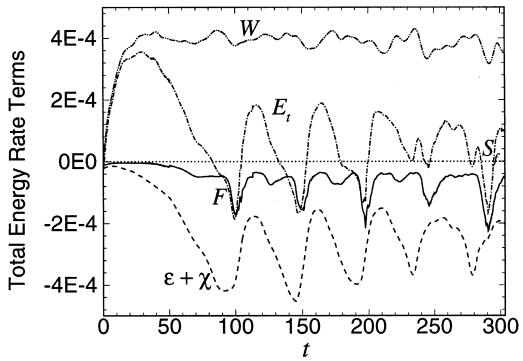

Figure 9. Volume integrals of the terms of the total energy equation: work input W, change in energy in time $E_{\rm t}$, dissipation rates ε and χ, filter dissipation rate F, buoyancy flux $B_{\rm f}$, flux of energy into sponge layer $S_{\rm f}$.

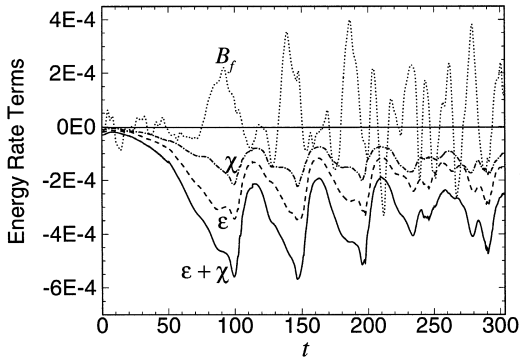

Figure 10. Buoyancy flux $B_{\rm f}$ and dissipation rates ε and χ, showing the transfer of potential to kinetic energy during periods of wave breakdown and turbulent dissipation.

flow features have emerged away from the boundary layer, as mixed boundary fluid progressively spreads into the interior stratified region and interacts with the oncoming waves.

Analysis indicates that the flow is quasi-periodic, going through a cycle of strong mixing and small-scale dissipation, followed by a quieter period of relaminarization and weaker dissipation. The volume integrals of the dissipation rates in Figures 8–10 show that the dissipation rates fluctuate throughout the mixing cycle. A first peak in dissipation occurs around t = 98 and subsequent peaks occur at approximately t = 147, 195, 234, and 290. The wave period for this flow is 39.2, approximately 20% shorter than the average duration between peaks in mixing.

It is not unexpected that the turbulent mixing cycle has a duration different from the wave period. Additional experiments for critical angle reflection over different bottom slopes ($3° < \alpha < 30°$) typically have mixing periods approximately 10–50% longer than the wave periods, but never shorter (Slinn and Riley, 1998b). The dissipation rate falls off rapidly after achieving its peak; from peak to trough takes approximately two buoyancy periods (from t = 100 to t = 115). This is consistent with other observations of the collapse time for episodic events of stratified turbulence (e.g., Hopfinger, 1987; Stillinger *et al.*, 1983). During the period of weakest dissipation, the flow restratifies and relaminarizes, i.e., the three-dimensionality of the flow decreases rapidly. The buildup to the second dissipation maximum takes longer (from t = 115 to t = 145) than the rate at which the turbulence collapses. During the buildup phase, the wave instabilities (static and dynamic) grow and develop before energy is strongly dissipated through turbulence. Thus, the system may respond sluggishly, as nonlinearities take time to develop and unstable modes grow at finite rates. The full wave breakdown cycle may be divided into six distinctive phases: (1) initial buildup of density gradients, (2) wave amplification and overturning, (3) growth of instabilities and onset of turbulence, (4) strong mixing, (5) decay of turbulence, and (6) restratification. Time scales for the growth rate of the instabilities, the decay time of the turbulence, and the time to restratify the boundary layer are not coupled to the wave period. For example, if the time for growth of the turbulence is too long, the flow could remain laminar. On the other hand, if the turbulence lasts too long, the fluid may become so well mixed near the boundary that it may not support oncoming internal gravity waves. As the turbulence decays, buoyancy forces act to restratify the boundary layer. Not until the boundary layer is reorganized does the next cycle of wave overturning and breakdown proceed. If wave amplification associated with critical angle reflection must wait for favorable conditions to reappear in the boundary layer, it is not surprising that the wave period and mixing period differ.

A possible contributing factor to the mixing period being longer than the wave period is that, through each mixing cycle, the background density gradient in the boundary layer region is weakened, which modifies the local buoyancy frequency N. Thus, as the next oncoming wave passes through the region, its angle of propagation may change, since ω is proportional to $N \cos\theta$ and ω should remain fixed. Thereby, the oncoming wave frequency no longer exactly matches the critical frequency associated with the bottom slope. Additional experiments (Slinn and Riley, 1998b) have shown that oncoming waves with frequencies close to (but not equal to) the critical frequency still break down into turbulence in nearly the same fashion as the critical angle cases. We have found that the mixing period increases when the oncoming waves propagate at a smaller angle than the bottom slope, as would occur when the density gradient weakens.

3.3. Instabilities

Two types of flow instabilities, convective and shear driven, are expected to contribute to turbulent wave breakdown. Convective instabilities are driven by the instantaneous density field, when heavier fluid is located above lighter fluid. Immediately prior to the growth of strong three-dimensionality, there are widespread overturns in the density field occurring across the breadth of the boundary layer. These overturns appear to be caused by a strong upslope flow, induced by the amplified shear of the oncoming wave as its energy density increases in the proximity of the bottom boundary.

Figure 3 above shows the density field in the boundary layer region at t = 88.5 (top), 93.7 (middle), and 102.2 (bottom). Overlaid on top of the isopycnals are shaded regions indicating the regions in which the flow is statically unstable. The unstable regions stretch across the breadth of the domain and are centered at a height of approximately $0.25\lambda_z$ away from the sloping boundary. They appear predominantly in this structure from about t = 90 to t = 100, for a time of approximately one-quarter of a wave period. Note that

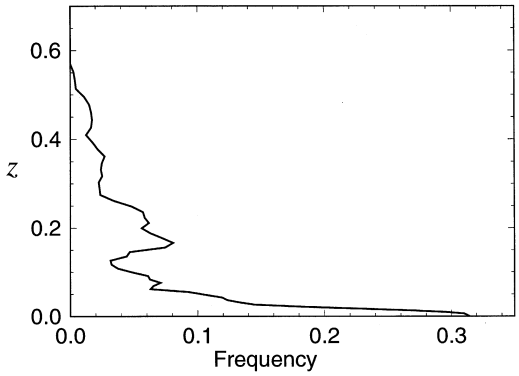

Figure 11. The frequency of overturned regions as a function of the distance from the wall.

the turbulence and wave overturning occur above the thermal front farther from the wall. Statistical analysis of the overturned regions of fluid indicates that the static instabilities all occur below a height of $0.56\lambda_z$ from the wall, and are present somewhere in the boundary layer region about 50% of the time. This result is typical of critical angle cases for a range of different slopes when Reynolds numbers are sufficiently high for transition to turbulence to occur.

Results for the frequency of occurrence of overturned regions, as a function of distance from the boundary, obtained from time integration over five mixing cycles are presented in Figure 11, showing the percentage of time in which a static instability was observed at each height. There are two prominent peaks in the figure. The dominant peak, located at the wall, is indicative of a very thin viscous sublayer in which the density stability structure is sensitive to small-scale perturbations. This is related to the boundary layer which is driven by the buoyancy imbalance associated with the no-flux boundary condition for the density field (Phillips, 1970). Throughout the wave period the near-wall region experiences both upslope and downslope flows. When the flow is upslope, heavier fluid from downslope is carried upslope. Closest to the wall the currents are reduced by viscosity and this upslope transport is also reduced. Thus, a thin layer of heavier fluid may develop slightly above the boundary. This does not necessarily lead to turbulence, however, because motions are inhibited by viscosity, especially due to the presence of the wall. Rather, laminar near-wall currents can be established, such as the backwash observed along the slope. This layer of frequent static instabilities near the wall is restricted to a region of thickness $0.05\lambda_z$ and occurs approximately 20–30% of the time.

The second major peak in Figure 11 is farther from the wall, centered at a height of approximately $0.17\lambda_z$. This peak reflects static instabilities related to turbulent wave breakdown. These instabilities occur approximately 8% of the time at a specified location. This is consistent with the approximate duration of the period of the mixing cycle consisting of initial wave overturning, prior to the period of strongest turbulence.

Shear-driven and convective instabilities are intrinsically related in a stratified flow. When shear-driven instabilities develop, leading to turbulence, they invariably develop regions of overturned fluid. Conversely, when (linear) wave amplification processes cause overturned regions, convective instabilities break down dynamically into a variety of unstable modes (Lombard, 1994). Hence, it is difficult to separate the influence of dynamic and static instabilities for breaking waves. The value of the local Richardson number is a commonly used criterion to identify stratified regions that may be dominated by shear-driven instabilities.

Shear instability is usually cited (e.g., Eriksen, 1978; Garrett and Munk, 1979) as the most likely means by which oceanic internal waves break down and generate fine-scale mixing. Garrett and Munk (1972) suggest that random superposition of different internal wave modes occasionally leads to regions with local Richardson number below 0.25, the value necessary for Kelvin–Helmholtz billows to develop in a steady parallel shear flow. In addition, other instabilities have been identified, such as Holmboe instabilities (Holmboe, 1962), which can occur at higher Richardson numbers than required for Kelvin–Helmholtz billows. Field measurements by Eriksen (1978) show that Richardson numbers in the range of 0.25 to 1.0 are frequently present in the open ocean.

Thorpe and Haines (1987) and Taylor (1993) observe that for internal wave reflection the initial wave instabilities originate from the location of the thermal front. We see similar initial flow features in the numerical experiments which we describe as lee waves riding behind the thermal front that are reminiscent

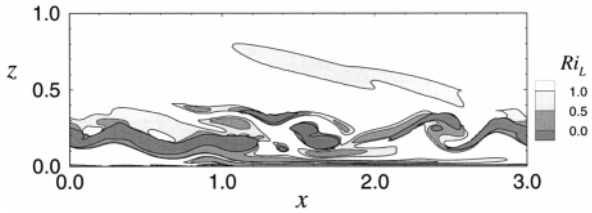

Figure 12. Contours of the local Richardson number at t = 96.8, as the wave instabilities develop, indicating regions of the flow that may be dynamically unstable. Contours of $Ri_{\mathrm{L}} < 0$ (dark grey), 0.5 (intermediate), and 1 (light grey) are shown.

of the early stages of Kelvin–Helmholtz billows in a parallel shear flow. Taylor's measurements suggest, however, that the initial large-scale wave overturns are primarily convectively driven.

Considerable attention in the literature has been focused on the critical Richardson number of 0.25, a value derived from the linear analysis of stratified, steady parallel shear flows. Differences exist, however, between instabilities in internal waves and in a shear layer oriented perpendicular to gravity. These differences make the critical value of 0.25 somewhat imprecise when applied to flows produced by internal waves. Orlanski (1972) and Delisi and Orlanski (1975) show that internal waves are unstable for Richardson numbers less than about 2. Significantly, Drazin (1977) and Meid (1976) show that even very small amplitude internal gravity waves (with corresponding large Richardson number) are unstable to small disturbances (through triad interactions). Lombard and Riley (1996) extend this analysis to finite amplitude gravity waves and show that the primary instabilities are three-dimensional and grow rapidly. For example, they show that a gravity wave with minimum local Richardson number of 7.2 (corresponding to initial wave amplitude one-half that of an overturning wave) and with Reynolds number 300 becomes unstable and breaks into turbulence within about four wave periods.

The local Richardson number, $Ri_L = N_L^2 / \left(\partial u/\partial z\right)^2$, gives a rough estimate of the ratio of the stabilizing effect of density stratification to the destabilizing effect of shear, and this can be used to identify dynamically unstable regions. Other definitions for a local Richardson number may be appropriate. For example, the shear in the direction of the wave-number vector could be used instead of the vertical shear, because it is more significant (and larger) in an internal wave. Another choice might be to include the influence of $\partial v/\partial z$. Strictly speaking the local Richardson number criteria is only appropriate for a parallel shear flow with a well-defined steady mean flow, whereas the unsteadiness of the wave reflection problem makes it imprecise to extend the theory to the time-dependent wave reflection process. Because the analysis herein is used to develop only qualitative and semiquantitative pictures of the relative importance of shear and convective instabilities, however, use of Ri_L as defined above should be adequate.

Local Richardson number contours of 0, 0.5, and 1.0 are shown for the center vertical plane ($y = 0.85\lambda_z$) in Figure 12 at t = 96.8. Negative values of Ri_{L} (darkest grey) correspond to the statically unstable regions. As can be seen from this figure, significantly larger proportions of the boundary layer region have $Ri_{\mathrm{L}} < 1$ (lightest grey) than are statically unstable ($Ri_{\mathrm{L}} < 0$). Details of these proportions are given below. Figure 12 suggests a strong correlation between dynamic and static instabilities since, as would be expected, the statically unstable regions are surrounded by regions with small positive values of local Richardson numbers. Additional analysis not presented here (i.e., simultaneous plots of Ri_{L}, $(\partial u/\partial z)^2$, and $\partial\rho/\partial z$) indicate that, during wave breakdown, regions with high shear values are more strongly correlated with regions of low Ri_{L} (less than 1) than are regions with low values of the density gradient.

The three-dimensionality of regions of dynamic instability is indicated by contours of Ri_{L} in Figure 13. Depicted are contours of Ri_{L} in a plane parallel to the wall within the turbulent boundary layer at $z = 0.24\lambda_z$ and t = 96.8. Here the abscissa is the x-axis and the ordinate is the y-axis (across-slope). Figure 13 shows that many of the overturned and dynamically unstable regions are small scale and three-dimensional.

The distribution of regions of low Richardson number may by quantified for this flow as a function of space and time. Figure 14 indicates the average spatial distribution in the z-direction of regions of Richardson numbers below 0, 0.25, 0.5, and 1.0 for the flow at t = 96.8. In this figure the abscissa indicates the distance from the wall and the ordinate indicates the fractional area at that height with Ri_{L} below the specified value. For example, at a height of 0.3 from the wall, approximately 30% of the flow has a negative Richardson number (i.e. is statically unstable), 35% has $Ri_{\mathrm{L}} < \frac{1}{4}$, 40% has $Ri_{\mathrm{L}} < \frac{1}{2}$, and 55% has $Ri_{\mathrm{L}} < 1$.

The dominant regions of low Ri_{L} associated with wave breakdown are located from $0.1\lambda_z < z < 0.4\lambda_z$. The region from $0.5\lambda_z < z < 0.8\lambda_z$ in which $Ri_{\mathrm{L}} < 1$ a significant fraction of the time, appear to be the

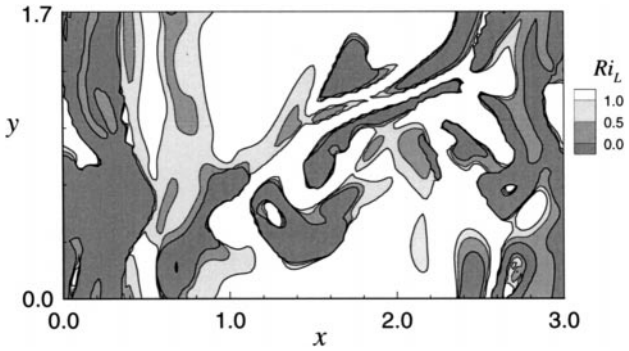

Figure 13. Contours of the local Richardson number in a plane parallel to the wall located in the turbulent boundary layer. The figure indicates some of the three-dimensional structure of the flow during this period and represents the plane at $z = 0.24\lambda_z$ for $t = 96.8$. The contours are for $Ri_{\rm L} < 0$ (dark grey), 0.5 (intermediate), and 1 (light grey).

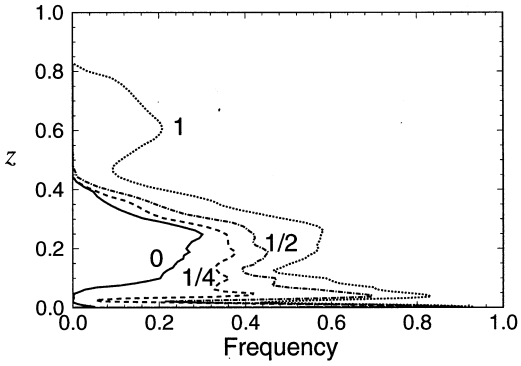

Figure 14. Percentage of volume with local Richardson numbers less than 0, 0.25, 0.5, and 1 as a function of height from the bottom wall at $t = 96.8$.

farthest from the boundary in which turbulence sometimes exists. The fraction of a control volume with low values of $Ri_{\rm L}$ is determined by defining functions G_R with $R = 0, 0.25, 0.5, 1.0$ that have values $G_R = 1$ if $Ri_{\rm L} < R$ and $G_R = 0$ if $Ri_{\rm L} > R$. Integrating the G_R's over the control volume (covering $z < \lambda_z$ at $t = 96$) shows that approximately 8% of the volume has $Ri_{\rm L} < 0$, 13% has $Ri_{\rm L} < \frac{1}{4}$, 18% has $Ri_{\rm L} < \frac{1}{2}$, and 32% has $Ri_{\rm L} < 1$.

The time evolution of the volume fractions with low $Ri_{\rm L}$ (determined from the G_R functions) are shown in Figure 15. As the flow develops, the familiar periodic behavior of strong mixing and dissipation, followed by a more stable situation, is evident. There is also suggestion over the first two mixing cycles that there are peaks in volume percentage of the Richardson numbers of 1, 0.5, and 0.25 somewhat before the peaks in volume percentage of the Richardson numbers less than zero (associated with static instabilities). For example, there appear to be local maxima of $Ri_{\rm L} < 1$ and $\frac{1}{4}$ at $t = 140$, followed by a peak in $Ri_{\rm L} < 0$ at $t = 150$.

This analysis of local Richardson numbers associated with the flow during periods of wave breakdown suggests that the wave field becomes dynamically unstable before significant regions of static instabilities develop, as larger regions with low $Ri_{\rm L}$ clearly develop before overturning occurs. We expect that there it is a combination of both types of instabilities at work that produce the net wave breaking dynamics. There is a complicated interaction between dynamic and static instabilities. Dynamic instabilities occur most frequently during the turbulent wave breakdown process, and can lead to statically unstable situations. As these develop, the static instabilities contribute to local regions of strong convection as available potential energy is released from local sources. A more complex stability analysis following the approach of Winters and D'Asaro (1994) which analyzes the transfer of energy from the "mean" flow to small-scale perturbations

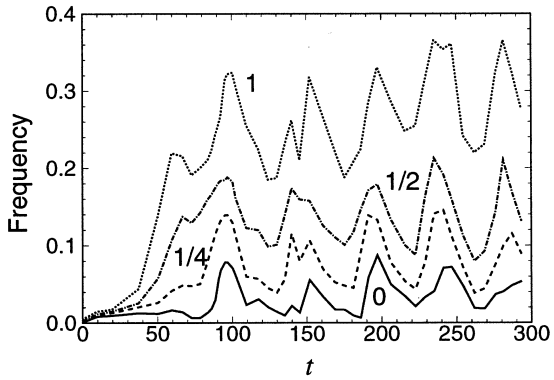

Figure 15. Percentage of volume of bottom vertical wavelength with local Richardson numbers less than 0, 0.25, 0.5, and 1 as a function of time.

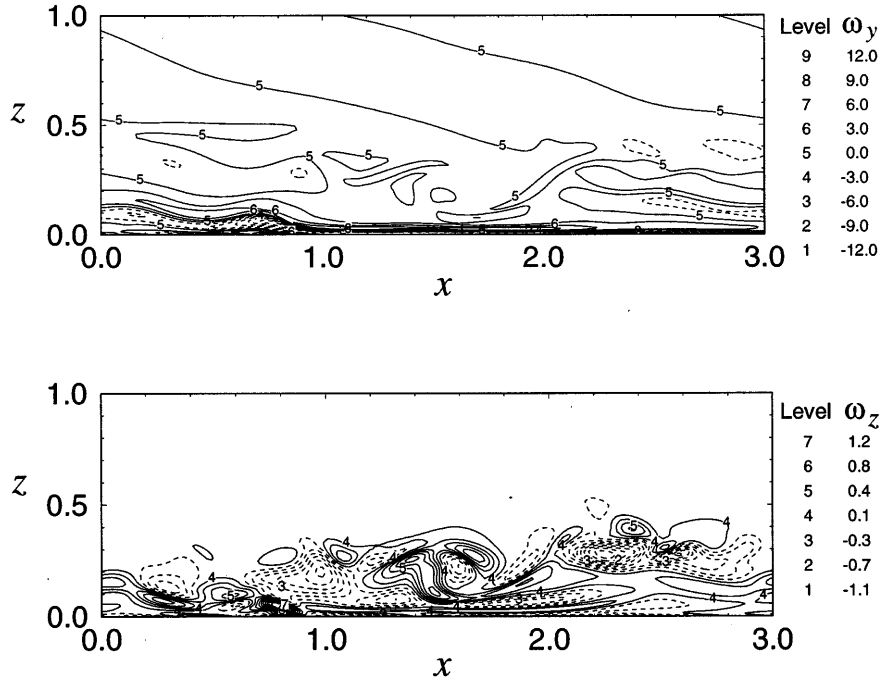

Figure 16. The vorticity components ω_y and ω_z in the plane of the slope at t = 93.7.

from buoyancy and shear production may be useful in future work if a satisfactory description of the mean flow can be achieved.

3.4. Vorticity Dynamics

An important characteristic of a turbulent flow is that it contains large amounts of vorticity. The Helmholtz vorticity equation describes the evolution of vorticity,

$$\frac{\partial \boldsymbol{\omega}}{\partial t} + \mathbf{u} \cdot \nabla \boldsymbol{\omega} = \boldsymbol{\omega} \cdot \nabla \mathbf{u} + \frac{\nabla \rho \times \nabla p}{\rho^2} + \nu \nabla^2 \boldsymbol{\omega}, \tag{3.1}$$

in which the first term on the right-hand side represents the change in the vorticity due to turning and stretching of vortex lines, the second term represents the generation of vorticity by baroclinic torque, and the third represents molecular diffusion of vorticity. In the Boussinesq approximation the background pressure gradient, the hydrostatic part, is much larger than the perturbation pressure gradient caused by local fluid accelerations, so that the baroclinic generation of vorticity occurs when density surfaces are displaced from their resting (horizontal) state.

Figure 16 shows the y and z_T components of vorticity, ω_y and ω_z, in the center plane (y = 0.85λ_z) of the computational domain at t = 94, where z_T is directed opposite the gravity vector. The only component of vorticity contained by the oncoming wave is ω_y. Examination of the contour levels in Figure 16 reveals that the ω_y component is much stronger than either ω_x (not pictured) or ω_z. There is a thin layer of large vorticity very near the bottom wall associated with the strong shear there. At the wall there is also a strong flux of vorticity into the flow. By the proximity of zero contours of ω_y very near the wall, however, it is evident that this vorticity from the boundary does not diffuse far into the domain, or alternatively, that the periodic production of positive and negative vorticity at the wall limits the effective depth of the diffusion. For linear wave reflection, near the wall the flow is similar to a Stokes flow (Cacchione and Wunsch, 1974), in which the boundary layer oscillates back and forth, upslope and downslope. For the linear case there is no net production of ω_y throughout the wave period, *i.e.*, there is equal production of positive and negative vorticity. Figure 16 shows that there is considerable ω_z of lower amplitude located at heights up to $z \approx 0.4\lambda_z$.

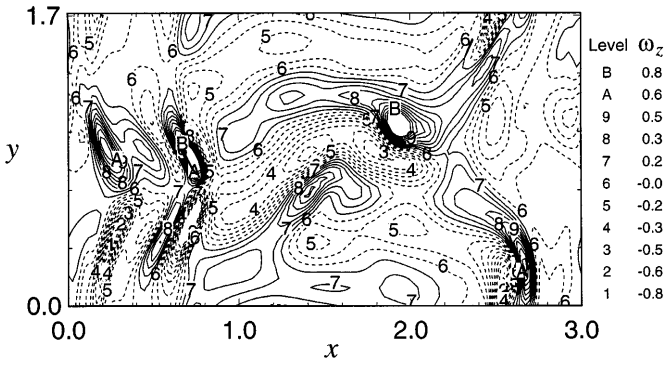

Figure 17. Vorticity component ω_z in a plane parallel to the slope located at a height $z = 0.07\lambda_z$ at $t = 93.7$.

Figure 17 shows a top view of ω_z in a plane parallel to the wall located at a height of $z = 0.07\lambda_z$. In this figure the strongest vorticity is located near the left-hand side of the domain near the thermal front (see Figure 3). The y-vorticity (not shown) is predominantly two-dimensional, with its strongest feature caused by shear from the upwelling flow over the thermal front. Also correlated with the location of the thermal front are the regions of strongest ω_x (the component in the x_T-direction, perpendicular to the gravity vector) and ω_z. These appear much more three-dimensional in nature, though approximately three times smaller than ω_y at this z and t. As time progresses, the regions of strongest vorticity and vorticity production move upslope together with the thermal front. At a greater distance from the boundary (e.g., $z = 0.25\lambda_z$) the vorticity magnitudes are comparable, indicating both that the sublayer vorticity has not extended this far from the wall and that turbulent mechanisms are dominant. The vorticity is strongest here where the flow is statically unstable (see Figure 3). Further analysis indicates that in this region both baroclinic generation and turning and stretching make large contributions to the vorticity.

Horizontal averages of the vorticity magnitudes as a function of z indicate that ω_y is the dominant component. The strongest vorticity is located near the boundary, and exists at enhanced levels out to approximately $z = 0.7\lambda_z$. Above this level, $z > 0.7\lambda_z$, all of the vorticity is from the oncoming wave. Outside of the viscous layer, the peak rms vorticity levels are approximately five times larger than that observed in the oncoming wave train. This enhancement is caused both by the increase in energy density from wave reflection, and by production of vorticity from turbulent effects. We note also that the magnitudes of ω_x and ω_z in the turbulent zone are approximately the same size as the magnitude of ω_y in the oncoming wave, before it reaches the turbulent zone.

The transfer and production of ω_x and ω_z are strongest in the regions where ω_y is largest, suggesting that there is a turning of vorticity from ω_y into the other components. Also evident is that the average values of ω_x are somewhat larger than ω_z ($|\omega_z| \approx 2\,|\omega_x|$) throughout the flow. It is significant that the bottom slope interferes with the development of large-scale horizontal structures containing significant amounts of ω_z. This is especially true in regions near the wall where the difference is most apparent.

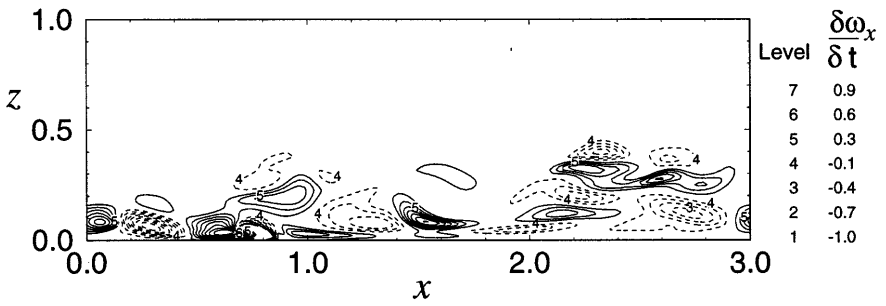

Figure 18. The baroclinic generation of ω_x in the plane of the slope at $t = 93.7$.

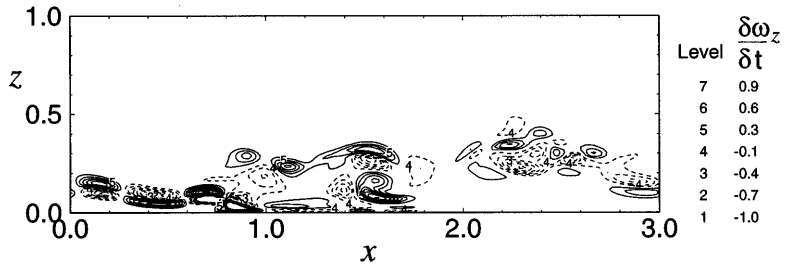

Figure 19. The contribution to the change of ω_z caused by turning and stretching of vortex lines due to turbulence in the plane of the slope at t = 93.7.

Figure 18 shows the x component of the baroclinic torque terms from the vorticity equation plotted at t = 93.7 (again refer to Figure 3). (There is no production of ω_z by this mechanism in the Boussinesq approximation.) The strongest regions of baroclinic generation of ω_x and ω_y are associated with the thermal front. Other regions located farther from the wall are also active in creating vorticity through this mechanism. Overall, the baroclinic generation of ω_y (not pictured) is stronger than the baroclinic generation of ω_x because of the relative strength of $\partial\rho/\partial x$ associated with the thermal front.

Finally, Figure 19 indicates the strength of the turning and stretching terms for the z_T component of the Helmholtz equation at t = 93.7. Here, the production of vorticity is strongest in the viscous sublayer where there is stronger vorticity to be manipulated. There are also significant increases in vorticity within the turbulent boundary layer away from the wall. Generally speaking the increase of vorticity from turning and stretching is stronger than baroclinic production for $z < 0.1\lambda_z$ and is comparable in magnitude with the production by baroclinic torque for $0.1\lambda_z < z < 0.5\lambda_z$, though each component of the production terms are functions of space and time.

3.5. Lower Reynolds Number Experiments

Four additional three-dimensional simulations were conducted at different Reynolds and Richardson numbers at the critical frequency over a bottom slope of 9.2°. The primary emphasis for the additional experiments was to study transition to turbulence. Case 1, presented above, was conducted at Re = 3600 and Ri = 46. The additional simulations (Cases 2–5) were conducted at Reynolds numbers of 2800, 2000, 1200, and 850 and Richardson numbers of 40, 43, 53, and 61, respectively. Figure 20 compares the volume averages of the shear components $(\partial w/\partial y)^2$ for these five simulations. These averages indicate when the wave breakdown becomes three-dimensional. Other measures, such as local dissipation rates, and the volume averages of v^2, are consistent with the indications of the development of three-dimensionality, and hence turbulence, from the mean square shear rates.

The lower Reynolds number simulations used a different geometry than for Case 1. The primary difference is that the forcing region is located farther from the bottom slope. Hence, the wave train begins to develop

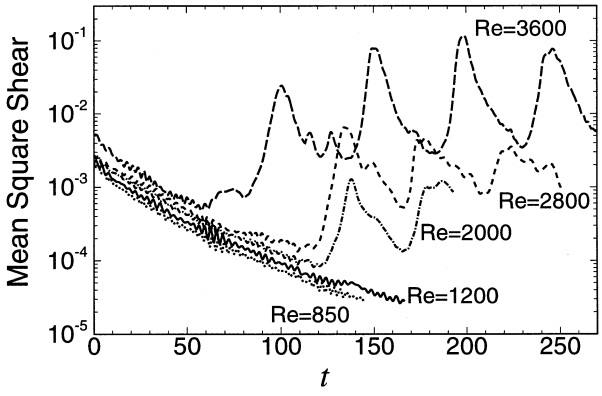

Figure 20. Transition to a three-dimensional (turbulent) flow occurs at a Reynolds number of approximately 1500 for the 9.2° bottom slope. Here the mean square shear quantity $(\partial w/\partial y)^2$ is plotted for simulations conducted at five different Reynolds numbers: 850, 1200, 2000, 2800, and 3600.

three-dimensionally at a later time, because it takes the wave longer to reach the bottom boundary. A second difference is that the ratio of the width of the wave forcing region to the vertical wavelength, determined by b in (2.10), was adjusted for Cases 2–5 to produce a steadier wave train (Slinn and Riley, 1998a).

Cases 2 and 3, with Re = 2800 and 2000, respectively, behaved very similar to Case 1. In all three cases, the waves transition and break down in very similar fashions, differing primarily in the intensity and duration of small-scale motions. In these experiments at lower Reynolds number, over 95% of the energy dissipation occurs at well-resolved spatial scales; consequently, effects of the hyperviscosity filter are negligible.

The Reynolds number was decreased until the three-dimensionality of the wave breakdown was suppressed. Note from Figure 20 that $(\partial w/\partial y)^2$ for Re = 1200 and Re = 850 continues to decay at t = 120. The three-dimensionality of the case at Re = 1200 is very weak and not readily apparent in $(\partial w/\partial y)^2$. The flow is very near transition and clear evidence of the increase in three-dimensional development of the wave is apparent in the $(\partial v/\partial z)^2$ shear (not shown). Case 4 is a transitional case, while Case 5 (Re = 850) is clearly laminar.

For the higher Reynolds number simulations the periodic nature of the intensity of the turbulence is apparent. Figure 20 shows that wave breakdown occurs at similar times for the cases with Re = 2800 and 2000. Peaks in the shear rates occur at t = 140 and 185, with a mixing period for each case of approximately 45 (compared with the wave period of 39.4).

Additional analysis (not shown) indicates that the reflected waves produce higher velocity currents in the boundary layer than occur in the oncoming wave train. The peak velocities in the boundary layer are approximately two to three times as large as the oncoming wave velocities for the two highest Reynolds number cases. The important point is that the ratio of the maximum velocity to the oncoming wave velocity is similar for the turbulent simulations. These results are consistent with laboratory measurement by Ivey and Nokes (1989), who observed maximum velocities of reflected waves of approximately two to three times the velocities of oncoming waves. This consistency should not be overemphasized, however, in view of differences in the wave amplitudes (Richardson numbers), wave generation mechanisms, and experimental geometries. Nonetheless, it is noteworthy that the maximum velocities occur approximately half a wave period before the peaks in dissipation.

A focus of these numerical experiments has been to determine the transition Reynolds numbers of the flow. The Reynolds number ($Re = U\lambda/\nu$) can be adjusted by changing the length scales, the velocity of the oncoming waves, or the viscosity. In order to resolve the small scales of motion in these experiments adequately, especially within the viscous boundary layer, the simulations have been conducted at moderate and low Reynolds number. The most successful way to observe turbulent breakdown is to have fairly large amplitude waves ($A > A_o/2$, where A_o is the amplitude of an overturning wave) approach the boundary. This approach differs somewhat from the laboratory experiments of Ivey and Nokes (1989) and Taylor (1993), who used relatively small amplitude waves ($A < A_o/5$). The global Richardson numbers, $Ri = \left(N\lambda/U\right)^2$, have been relatively low (30–300) for most of the turbulent simulations, compared with those used in laboratory experiments ($Ri \sim$ 10,000). The Reynolds numbers of the numerical experiments (300–4,000), however, are comparable with the laboratory values (2,000–8,000), but they are achieved using larger amplitude waves in a more viscous fluid.

3.6. Turbulent Layer Thickness

Determination of a practical measure for the thickness of the turbulent layer, δ_T, is considerably more complicated for the wave reflection problem than for simpler types of boundary layer flows. For example, a standard measure of δ for flow over a flat plate is the height to where the boundary layer velocity is $0.99U_\infty$, where U_∞ is the free stream velocity. But the wave-driven flows in this study are different. Velocities in the turbulent layer are typically two to three times *higher* than the "free stream" velocities (where free stream velocities refer to current speeds of the oncoming wave field). In addition, the transition zone (e.g., $\lambda_z/3 < z < 2\lambda_z/3$) between the turbulent layer and the oncoming wave field is temporally and spatially variable. Further complexity is added when reflected gravity waves from the turbulence propagate upward, passing through and interacting with downward propagating waves. These, and other factors, complicate defining a measure of the turbulent layer depth. One of the advantages in attempting the determination,

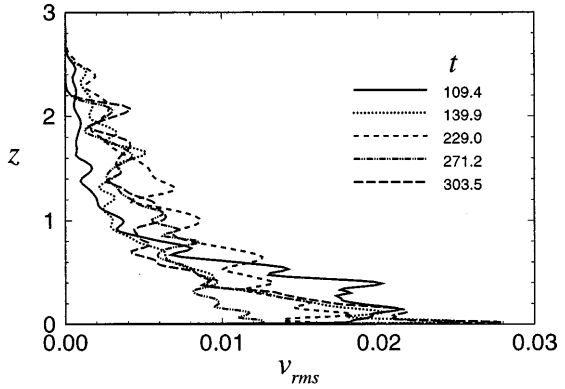

Figure 21. The integrated rms v-velocity component as a function of height in planes parallel to the slope at different times for Case 1.

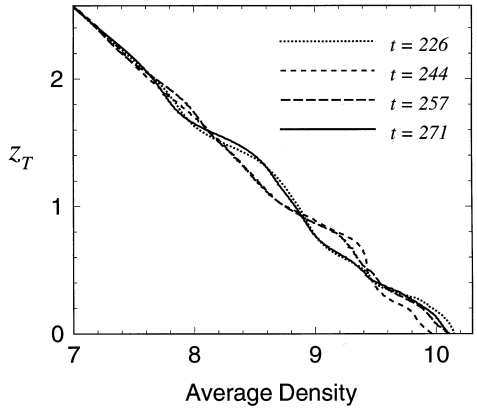

Figure 22. Horizontally averaged density profiles for Case 1 at t = 226, 244, 257, and 271.

however, is that the oncoming waves are two-dimensional. Consequently, the variability in the y-direction distinguishes incident waves from responses produced in the turbulent layer.

A variety of methods have been used to determine the thickness of the turbulent layer for the simulations described herein. Figure 21 shows the rms v-velocity component as a function of z for Case 1 at various times. The main point of the figure is that the three-dimensionality and turbulence occur in the near wall region within a "layer" of approximate thickness $\delta_T \approx \lambda_z/2$. The v-velocity located significantly above δ_{T} (e.g., $z > \lambda_z$) is primarily associated with gravity waves reflected from the turbulent region. Additional indications of the thickness of the turbulent layer are apparent in Figures 3, 11, 12, 14, and 16-19 above in relation to flow instabilities and vorticity dynamics. Each of these measures indicate that the best estimate of the thickness of the turbulent layer is $\delta_{\mathrm{T}} \approx \lambda_z/2$.

3.7. Changes to Background Field

An issue of considerable interest, with regard to the model problem and its oceanic counterpart, is the long term response of the background, when modified by wave breakdown and mixing in the boundary layer. Two significant results that may appear are changes to the background density profiles and creation of mean currents. Each of these flow adjustments are indicators that net mixing effects are communicated to the interior stratified fluid. Indications of net changes to the background fields were suggested in Figure 7 by the volume integrals of the kinetic, potential, and total energies, which showed increases with time, indicating increased currents (kinetic energy), changes to the background density stratification (potential energy), and reflected waves (both kinetic and potential energy).

Profiles of the horizontally (perpendicular to gravity) averaged density for Case 1 are shown in Figure 22 at t = 226, 244, 257, and 271 as a function of z_T (parallel to gravity). An arbitrary reference value for the constant background density, ρ_0 = 10 at z_T = 0, has to be added in Figure 22 to form the total density field before averaging the values, i.e., $\rho_{\mathrm{t}} = \rho_0 + z_T \partial\overline{\rho}/\partial z_T + \rho$. The (x, y, z) and (x_T, y, z_T) coordinate systems intersect at the origin $(0, 0, 0)$. The horizontal averaging process nearly eliminates the density structure of the oncoming waves which are periodic in x but only approximately periodic in x_T. Horizontal averaging is done on the intervals $0 \le y \le 1.7\lambda_z$ and $0 \le x_T \le \lambda_x$ for $z_T > \lambda_x \sin\alpha$, and for $0 \le x_T \le x_W$ for $z_T < \lambda_x \sin\alpha$ where $x_W = z_T/\tan\alpha$ is the location of the sloping boundary.

The initial density profiles ($t < 60$, not shown) are approximately linear when only oncoming waves are present. After three to four mixing cycles adjustments to the initial profile have reached a height of at least $z_T = 2\lambda_z$. While the variability in the lower region ($z_T < 0.5\lambda_z$) may be attributed to the temporal phase of the upslope/downslope flow and the stage of mixing, changes in the density profile above $z_T = 0.5\lambda_z$ represent transport of the mixed fluid into the stably stratified interior.

By t = 226 layering of the mean density profile is evident. The profiles at t = 226 and 271 are similar to each other, as are the profiles at t = 244 and 257. At t = 244 (and 257) for $0.4\lambda_z < z_T < 0.8\lambda_z$, the density gradient is much weaker than the original linear profile. Associated with this layer is an intrusion

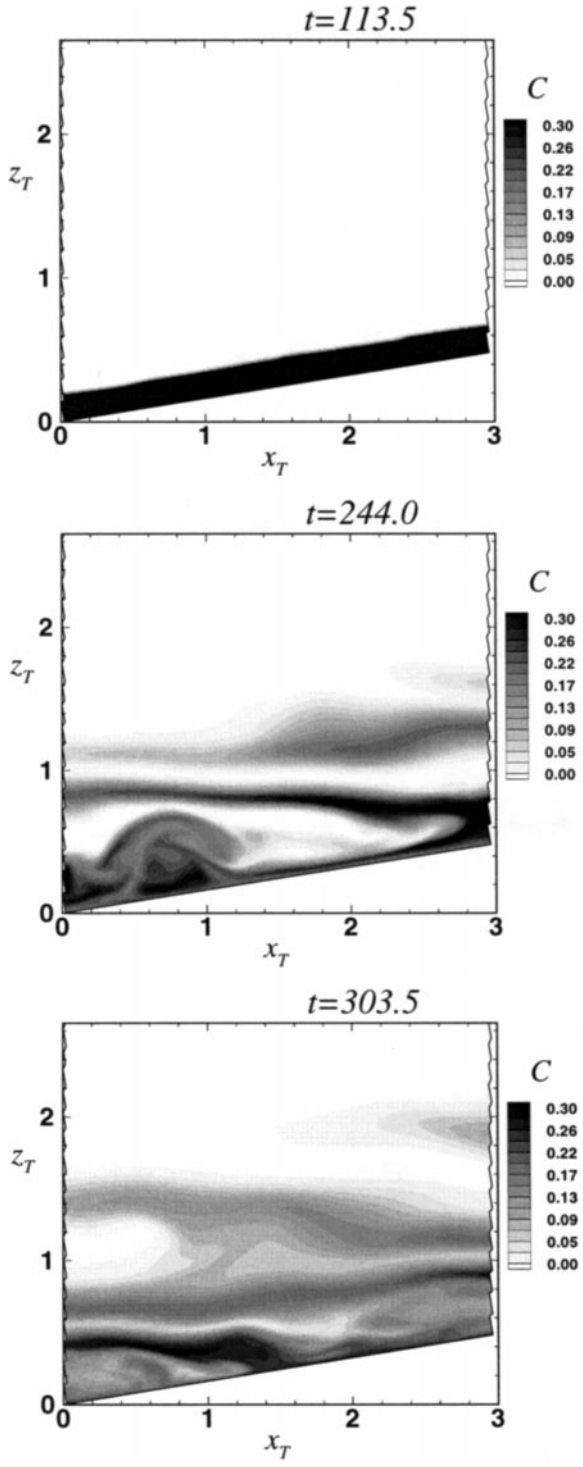

Figure 23. Dye field concentrations at t = 113, 244, and 303.

of mixed fluid that propagates into the interior stratified region from the boundary layer. Above the more homogeneous layer is a layer $0.8\lambda_z < z_T < 1.0\lambda_z$ (at t = 244) of increased density gradient. For t = 271 (and 226) the most homogeneous mixed layer is observed at $0.8\lambda_z < z_T < 1.2\lambda_z$, and the density structure exhibits layering to heights approaching z_T = 2.0.

Additional evidence of the layering of the fluid is revealed in Figure 23. Here, a passive "dye" has been released in the near wall region at t = 113, after the flow has gone through the first mixing cycle,

and is followed through four mixing cycles. The initial concentration, C, of the dye near the boundary is C = 1.0 for $z < 0.15\lambda_z$, falling off linearly between $0.15\lambda_z < z < 0.25\lambda_z$, and C = 0 for $z \geq 0.25$. As mixing occurs in the turbulent layer the concentration of dye near the wall decreases. Contour levels of $0 < C < 0.3$ are plotted in Figure 23 at t = 113, 244, and 303. A horizontal intrusion of dye is observed to steadily work its way into the interior domain, approximately following surfaces of constant density. At t = 244 two distinct horizontal dye layers are evident, located at $z_T \approx 0.8\lambda_z$ and $z_T \approx 1.2\lambda_z$. These two layers are actually a single horizontal intrusion crossing the periodic boundaries. Thus by t = 244, approximately 3.5 wave periods after being released, the dye has extended over two horizontal wavelengths into the interior flow from the turbulent boundary layer. By t = 303 the location of the upper dyed layer appears to have become raised to $z_T \approx 1.4\lambda_z$. This response, however, is due to the motion of the oncoming internal wave through the intrusion of dyed fluid, and occurs in a reversible fashion, lifting and falling through different phases of the oncoming wave. Two important points are revealed by the motion of the dye. First, the change in the location of the homogeneous mixed layer observed in Figure 22 above is explained. The oncoming wave causes the depth of the mixed layer to oscillate. Second, mean currents induced by the breaking waves are revealed. There is a steady circulation driven by buoyancy forces as fluid of intermediate density is created through boundary mixing and spreads into the interior along constant density surfaces. These induced currents contribute to the increase of kinetic energy in the control volume shown in Figure 7. We conclude that the net effects of boundary mixing are not confined to the boundary layer region but are communicated horizontally to the interior stratified fluid.

3.8. Mixing Efficiencies

A quantity of particular interest is the mixing efficiency, which is related to the portion of wave energy that goes into irreversible mixing of the density field. In the present numerical experiments, the mixing efficiency is represented as the ratio of the potential energy dissipated to the work input to generate the oncoming waves,

$$\eta = \frac{-\int_{t_i}^{t_f} [\chi + F_{\mathrm{PE}}]\, \mathrm{d}t}{\int_{t_i}^{t_f} W\, \mathrm{d}t}. \tag{3.2}$$

The values of χ and W are integrated over the full domain from the time when the oncoming wave train has reached the boundary, t_{i}, until the end of the simulation, t_{f}.

Because χ oscillates throughout the mixing cycle, while the work input remains almost constant, the resulting value of η oscillates about a mean value over each mixing cycle, but the oscillations dampen in time as the respective integrals become larger. For Case 1 the ratio of the integrals of $-[\chi + F_{\mathrm{PE}}]$ and W quickly achieves a stable value of η = 0.32 after the wave train reaches the boundary. For each of the simulations, the best approximation for t_i was chosen based upon energetics and flow visualizations, and the sensitivity of the result on η was examined to arrive at a best estimate for the mixing efficiency.

Table 1 presents the mixing efficiencies, heat-gain coefficients, and radiation coefficients for Cases 1–5. The heat-gain coefficient is defined, similar to the mixing efficiency, as the ratio of the integrals of the kinetic energy dissipation rate to the work input,

$$H = \frac{-\int_{t_i}^{t_f} [\varepsilon + F_{\mathrm{KE}}]\, \mathrm{d}t}{\int_{t_i}^{t_f} W\, \mathrm{d}t}. \tag{3.3}$$

The radiation coefficient, R, is inferred from the remainder of energy not dissipated as either heat or mixing, i.e., $R = 1 - \eta - H$. For these critical angle simulations, carried out over a range of Reynolds numbers, the mixing efficiencies vary between 0.32 and 0.38. Thus, a typical energy budget for the oncoming waves is that approximately 35% of the oncoming wave energy goes into mixing the stratified fluid, approximately 50% is dissipated as heat, and approximately 15% of the incident energy is reradiated away from the turbulent boundary layer by smaller-scale gravity waves or induced mean currents.

The error bars on the results are approximately ± 0.01 based upon the subjectivity introduced by choosing t_{i} and t_{f} for the integrations of χ and W. There is no obvious dependency of the mixing efficiency on the Reynolds number. While one might assume that higher Reynolds number flows should generally be more

Table 1. Energy Budgets at Critical Angle

Case	Slope	Re	Mixing	Heat	Radiate
1	9.2	3600	0.32	0.56	0.12
2	9.2	2800	0.37	0.48	0.15
3	9.2	2000	0.36	0.45	0.19
4	9.2	1200	0.38	0.50	0.12
5	9.2	850	0.36	0.58	0.06

efficient at mixing, analysis to be presented separately (from Slinn, 1995) suggests that low Reynolds number (laminar) internal waves have mixing efficiencies of 0.5 (for a Prandtl number of 1). Thus, separating laminar from turbulent dissipation rates is ineffective in the simulations.

4. Summary

Results from numerical experiments of the nonlinear flow development due to internal wave reflection from a critical bottom slope have been presented. These experiments are representative of critical angle reflection for slopes shallower than about 15°. The simulations have demonstrated that oncoming waves at the critical frequency break down into a turbulent layer of approximate thickness $\lambda_z/2$ when they reflect from the bottom topography. The turbulence is cyclical in nature, going through a mixing phase approximately once in 1.2 wave periods. A quasi-steady state develops in which the oncoming wave energy accumulates and then is dissipated near the wall while adjusting the background density profile. The results from the kinetic energy balance indicate that there is a strong positive buoyancy flux of energy from the available wave potential energy into kinetic energy.

Between mixing cycles, the boundary layer relaminarizes and restratifies and sets up a flow field whose most defining feature is a thermal front, which moves upslope at the x component of the phase speed of the oncoming wave. The thermal front is not characterized by steady localized mixing, as in the turbulent bore observed by Ivey and Nokes (1989) for a 30° slope. The flow development more closely resembles the periodic flow behavior observed by Taylor (1993) over a 20° slope. Other flow features are in qualitative agreement with related laboratory studies, and show similar development of features such as current velocities, turbulent layer thicknesses, flow dynamics, and transition Reynolds numbers.

The dynamics of wave breakdown appear to be primarily associated with local upslope/downslope flow induced by the oncoming wave. A prominent feature of the energetics is a strongly oscillating buoyancy flux, indicative of the upslope/downslope flow that occurs twice per wave period. It appears that the upslope flow, generated in a particular phase of the oncoming wave interacting with the presence of the boundary, is responsible for setting up wave overturning that leads to subsequent breakdown into turbulence.

Transition to turbulence occurs at approximately $Re = 1500$. The turbulence in the boundary layer reflects energy upward across the path of the oncoming internal waves, contributing to mixing away from the boundary. Changes to the background density profile and the generation of intrusions of mixed fluid occur in regions significantly farther from the wall than the depth of the turbulent boundary layer. Mixed fluid is advected horizontally more than two wavelengths away from the boundary layer within a few wave periods. Critical angle reflection is an effective means of dissipating the oncoming wave energy, and, in these experiments, approximately 85% of the wave energy is dissipated in the boundary layer, into heat and mixing of the background density profile. The dynamics of internal wave reflection away from the critical angle will be investigated further in a separate paper.

References

Batchelor, G.K. (1967) *An Introduction to Fluid Dynamics,* Cambridge University Press, Cambridge, 615 pp.

Cacchione, D.A., and Drake, D.E. (1986) Nepheloid layers and internal waves over continental shelves and slopes, *Geo-Marine Lett.,* **6**, 147–152.

Cacchione, D.A., and Southard, J.B. (1974) Incipient sediment movement by shoaling internal gravity waves, *J. Geophys. Res.*, **79**, 2237–2242.
Cacchione, D., and Wunsch, C. (1974) Experimental study of internal waves over a slope, *J. Fluid Mech.*, **66**, 223–239.
Delisi, D.P., and Orlanski, I. (1975) On the role of density jumps in the reflection and breaking of internal gravity waves, *J. Fluid Mech.*, **69**, 445–464.
Drazin, P.G. (1977) On the instability of an internal gravity wave, *Proc. Roy. Soc. A*, **356**, 411–432.
Durran, D.R., Brown, R., Slinn, D.N., and Yang, M.J. (1993) Towards more accurate wave-permeable boundary conditions, *Mon. Weather Rev.*, **121**, 604–620.
Eriksen, C.C. (1978) Measurements and models of fine structure, internal gravity waves, and wave breaking in the deep ocean, *J. Geophys. Res.*, **83**(C6), 2989–3009.
Eriksen, C.C. (1982) Observations of internal wave reflection off sloping bottoms, *J. Geophys. Res.*, **87**(C1), 525–538.
Eriksen, C.C. (1985) Implications of ocean bottom reflection for internal wave spectra and mixing, *J. Phys. Ocean.*, **15**(9), 1145–1156.
Eriksen, C.C. (1998) Internal wave reflection and mixing at Fieberling Guyot, to appear in *J. Geophys. Res. Oceans*
Garrett, C., and Munk, W. (1972) Oceanic mixing by breaking internal waves, *Deep-Sea Res.*, **19**, 823–832.
Garrett, C., and Munk, W. (1979) Internal waves in the ocean, *Ann. Rev. Fluid Mech.*, **11**, 339–369.
Gilbert, D., and Garrett, C. (1989) Implications for ocean mixing of internal wave scattering off irregular topography, *J. Phys. Ocean.*, **19**, 1716–1729.
Gordon, R.L. (1980) Boundary layer under near-inertial internal waves over a critically sloping bottom, *J. Phys. Ocean.*, **10**, 1032–1038.
Holmboe, J. (1962) On the behavior of symmetric waves in stratified shear layers, *Geofys. Publ.*, **24**, 67–113.
Hopfinger, E.J. (1987) Turbulence in stratified fluids: A review, *J. Geophys. Res.*, **92**(C5), 5287–5303.
Ivey, G.N., and Nokes, R.I. (1989) Vertical mixing due to the breaking of critical internal waves on sloping boundaries, *J. Fluid Mech.*, **204**, 479–500.
Lele, S.K. (1992) Compact finite difference schemes with spectral-like resolution, *J. Comput. Physics*, **103**, 16–42.
Lombard, P.N. (1994) The stability of finite amplitude gravity waves, Ph.D. Thesis, University of Washington, 161 pp.)
Lombard, P.N., and Riley, J.J. (1996) On the breakdown into turbulence of propagating internal waves, *Dynamics Atmos. Oceans*, **23**, 345–356.
MacCready, P., and Rhines, P.B. (1991) Slippery bottom boundary layers on a slope, *J. Phys. Ocean.*, **23**, 5–22.
Meid, R.R. (1976) The occurrence of parametric instabilities in finite-amplitude internal gravity waves, *J. Fluid Mech.*, **78**, 763–784.
Orlanski, I. (1972) On the breaking of standing internal gravity waves, *J. Fluid Mech.*, **54**, 577–598.
Phillips, O.M. (1970) On flows induced by diffusion in a stably stratified fluid, *Deep-Sea Res.*, **17**, 435–443.
Phillips, O. M., (1977) *The Dynamics of the Upper Ocean*, 2nd edn., Cambridge University Press, Cambridge, 336 pp.
Slinn, D.N. (1995) Numerical simulation of turbulent mixing caused by internal wave reflection from sloping boundaries, Ph.D. Dissertation, University of Washington, 398 pp.
Slinn, D.N., and Riley, J.J. (1996) Turbulent mixing in the oceanic boundary layer caused by internal wave reflection from sloping terrain" *Dynamics Atmos. Oceans*, **24**, 51–62.
Slinn, D.N., and Riley, J.J. (1998a) A model for the simulation of turbulent boundary layers in an incompressible stratified flow, to appear in *J. Comput. Phys.*
Slinn, D.N., and Riley, J.J. (1998b) Internal wave reflection from sloping boundaries, submitted to *J. Fluid Mechanics.*
Stillinger, D.C., Helland, K.N., and Van Atta, C.W. (1983) Experiments on the transition of homogeneous turbulence to internal waves in a stratified fluid, *J. Fluid Mech.*, **131**, 91–122.
Taylor, J.R. (1993) Turbulence and mixing in the boundary layer generated by shoaling internal waves, *Dynamics of Atmos. and Oceans*, **19**, 233–258.
Thorpe, S.A., and Haines, A.P. (1987) On the reflection of a train of finite-amplitude internal waves from a uniform slope, *J. Fluid Mech.*, **178**, 279–302.
Thorpe, S.A. (1989) The distortion of short internal waves produced by a long wave, with application to ocean boundary mixing, *J. Fluid Mech.*, **208**, 395–415.
Thorpe, S.A. (1992) Thermal fronts caused by internal gravity waves reflecting from a slope, *J. Phys. Ocean.*, **22**, 105–108.
Thorpe, S.A. (1997) On the interactions of internal waves reflecting from slopes, *J. Phys. Ocean.*, **27**, 2072–2078.
Turner, J.S. (1973) *Bouyancy Effects in Fluids*, Cambridge University Press, Cambridge, 368 pp.
Winters, K.B. (1989) Intensification and instability of internal gravity waves at caustics and critical levels, Ph.D. Thesis, University of Washington, 194 pp.
Winters, K.B., and D'Asaro, E.A. (1994) Three-dimensional wave instability near a critical level, *J. Fluid Mechanics*, **272**, 255–284.
Winters, K.B., Lombard, P.N., Riley, J.J., D'Asaro, E.A. (1995) Available potential energy and mixing in density stratified fluids, *J. Fluid Mech.*, **289**, 115–128.